PHYSICAL REVIEW E **95**, 063112 (2017)

Instability evolution of the viscous elliptic liquid jet in the Rayleigh regime

Shibo Gu, Lipo Wang,* and David L. S. Hung
UM-SJTU Joint Institute, Shanghai Jiao Tong University, Shanghai, China

(Received 10 March 2017; published 21 June 2017)

For jet flow emanating from noncircular orifices, an unbalanced surface tension force leads to capillary instability, which is independent of influence from the ambient air in the Rayleigh regime. In the present article, the dynamic behavior of incompressible elliptical jets in the Rayleigh regime is investigated. Theoretically, with the consideration of the fluid viscosity, the solution of the Cosserat equation consists of a particular solution and a complementary solution. For the complementary solution the wave number of disturbance modes has two complex conjugate roots, which are responsible for the jet breakup. To match the nonzero particular solution, a spatial wave needs to be introduced, which is independent of external perturbations. Physically, such a spatial wave is interpreted as the axis-switching phenomenon. The predicted features of the axis-switching wavelength and the damping effect from the fluid viscosity have been successfully verified by experimental results. Moreover, the dispersion relations from the present theory suggest that the growth rate of spatial instability is influenced by orifice eccentricity, the Weber number, and the Ohnesorge number.

DOI: 10.1103/PhysRevE.95.063112

I. INTRODUCTION

Liquid interface dynamics is of both fundamental and practical importance. For example, at the jet interface, the instability evolution, momentum, and species mixing are closely relevant to atomization and spray. Physically, once the instability modes, which may originate either from natural sources or forced perturbations imposed on the jet system, are strong enough, the jet breaks up. According to Reitz [1], there are four different jet instability and breakup regimes, which are the Rayleigh regime, first wind-induced regime, second wind-induced regime, and atomization regime. Such a classification depends on the relative dominance of the liquid inertia, surface tension, and aerodynamic forces acting on the jet, which can be summarized in the nondimensional Weber number $\mathrm{We}_L = U^2 R \rho_L / \sigma$ for the liquid phase and $\mathrm{We}_G = U^2 R \rho_G / \sigma$ for the gas phase, where U is the uniform jet velocity, R is the equivalent radius calculated from the jet cross-section area, ρ_L and ρ_G are the liquid and gas density, respectively, and σ is the surface tension coefficient. Under some conditions, the gravity force and liquid viscous forces are important as well.

The pioneering works on interface instability analysis include the study of liquid sheet dynamics [2] and interface instability [3–6]. For instance, Rayleigh studied the classic circular jet problem in the Rayleigh regime [4], where the effect of aerodynamics on the liquid jet can be neglected. Under the inviscid liquid assumption, the velocity potential satisfies the Laplacian equation. If the gravity effect is negligibly small, jet disintegration is mainly due to surface tension, referred to as capillary instability. The solution of the linearized equation for the axisymmetric disturbance component suggests that the liquid jet will break up when the disturbance wavelength exceeds the jet circumference. The linear Rayleigh theory developed for small perturbations is capable of a rather accurate prediction of the breakup time and length of capillary jets of low-viscosity liquids [7].

Besides the circular case, jets from different orifices are important as well, because of the advantages in mixing enhancement, faster breakup, and more freedom for design and control. In comparison with the aforementioned extensively studied circular jet problem, nonsymmetric jets are less understood, especially the axis-switching phenomenon, which originates from the imbalance between the capillary force and inertia force, leading to a change of the cross-section shape along the jet flow direction. Most of the existing results on nonsymmetric jet flows have been obtained either experimentally or numerically [8–10]. For example, the effects of the orifice aspect ratio and liquid viscosity on the axis-switching process of an elliptical jet were investigated experimentally [8]. It has been found that the breakup of an elliptic liquid jet is largely influenced by the shape of the orifice.

The relatively tractable elliptic configuration is of special interest for analysis. For the inviscid case, three-dimensional equations can be solved with the velocity potential method [4]. However, for the viscous case, an exact three-dimensional solution has not yet been obtained. Alternatively, one-dimensional Cosserat equations are derived to approximate the elliptical jet dynamics based on the assumption of a negligible cross-section variation [11,12]. For the circular case, when setting the semimajor and semiminor axes equal, the solution of such Cosserat equations agrees well with Rayleigh's results [4]. The mean velocity profile inside the elliptic jet was introduced and the propagation of different disturbances was analyzed in Refs. [13,14]. Bechtel and Bechtel *et al.* [15,16] studied the motion of inviscid and Newtonian elliptic jets directly from the Navier-Stokes equations. By integration over the cross section, one-dimensional equations with the same form as the Cosserat equations can be obtained. In addition, the effects of viscosity and gravity have been partly discussed. Amini *et al.* used the Cosserat model to study the growth rate of forced disturbances, and the dependence on different characteristic parameters [17,18]. Subsequently, the jet breakup property, together with experimental results, have been discussed, but the perturbation growth rate and cutoff wave number seem to have been significantly overpredicted [19]. For more complex cases, the three-dimensional

---

*lipo.wang@sjtu.edu.cn

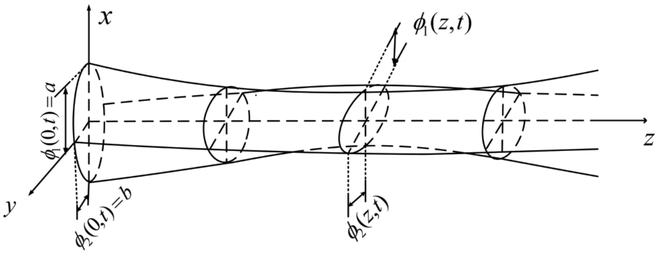

FIG. 1. Illustration of an elliptic jet configuration. Because of the unbalanced capillary force, the major axes change along the jet flowing direction z, called the axis-switching phenomenon.

perturbation dynamics of the inviscid elliptic jet interacting with the surrounding gas was investigated. Predictions from the theoretical model are meaningful in quite broad parameter regimes [19].

Based on the existing literature results, to our knowledge, this important fluid mechanics problem is not yet well understood. Some key issues related to the detailed features of the nonsymmetric jets need to be analyzed systematically from the control equations. Especially, the influence from the fluid viscosity, which is of fundamental importance for both fluid dynamics and applications, has been seldom systematically investigated. The present article focuses on the instability evolution in the initial range before jet breakup, the jet axis-switching, and the effects of relevant parameters on disturbances. Meanwhile, the results from theoretical derivations and experimentations are compared for verification.

II. STABILITY ANALYSIS

A. Flow configuration

The problem to be analyzed is illustrated in Fig. 1. Considering a liquid jet emanating from an elliptical orifice, in the Cartesian coordinate system, x and y denote the directions along the principal axes, and z is the jet flow direction. Under the action of an unbalanced capillary force, the jet axes $\phi_1(z,t)$ and $\phi_2(z,t)$ change both spatially along z and temporally with t, which then leads to a jet cross-section change in a periodic manner, and thus the axial velocity $v(z,t)$ as well. Such a phenomenon is referred to as axis-switching, which is one of the most noticeable features of nonsymmetric jets.

Figure 2 shows a comparison of experimental observations for the circular and elliptic jet cases, respectively. At the same jet pressure and the same jet cross-section area, from the side view, the photograph of the structure shows clearly the oscillation of the major axis. In an initial range with a limited flowing distance the circular jet shape remains almost constant, while the cross section of the elliptic jet oscillates periodically. Such an axis-switching process continues until jet breakup or other disturbance modes become strong enough to alter the jet structure.

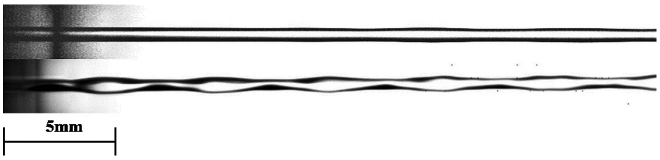

FIG. 2. Experimental observation showing the structure difference of the liquid jet from a circular (above) and elliptical (below) orifice. For comparison, the experimental conditions are well controlled. For both cases, the jet pressure is 7 kPa and the equivalent cross-section area remains the same as well.

B. Problem definition

For the nonsymmetric jet problem with complex orifices, it becomes mathematically difficult, even intractable, to apply the three-dimensional Navier-Stokes equations to obtain an analytical solution. Therefore, it is necessary to reasonably simplify the problem. Lee [20] neglected all radial inertia and viscous effects and derived a nonlinear one-dimensional set of equations for inviscid, incompressible circular jets based on three-dimensional Navier-Stokes and continuity equations. A well-accepted Cosserat model equation is based on the one-dimensional continuum model to formulate the material curve with two deformable directors representing the cross section of the jet [11,12,21–23]. The important inertial force, capillary force, and viscous force have been reasonably modeled, which can be justified by the equation solution. For instance, it has been shown [24] that the breakup length and its dependence on relevant parameters can be fully predicted. Bogy [25,26] concluded that one-dimensional Cosserat equations are suitable for describing many instability features with preference to Lee's equations. Moreover, Bechtel *et al.* [15] derived a lower-dimensional model systematically from the Navier-Stokes equations, which results in the same Cosserat equations if only the leading order terms are considered. According to the preset characteristic parameters, the jet is in the Rayleigh regime with negligible influences from gravity and the ambient gas [1]. Therefore, the Cosserat equation is adopted as the model equation in the present analysis.

The continuity equation can be written as

$$\zeta_1 + \zeta_2 + v_z = 0, \tag{1}$$

where v_z is the derivative of the axial velocity $v(z,t)$ with respect to z, and ζ_1 and ζ_2 satisfy the following relations,

$$\phi_{1t} + v\phi_{1z} - \phi_1\zeta_1 = 0, \quad \phi_{2t} + v\phi_{2z} - \phi_2\zeta_2 = 0. \tag{2}$$

Equation (1) shows the kinematic condition of zero net mass flux across the jet interface.

The Cosserat momentum equations in the x,y,z directions are

$$\begin{aligned}
&\tfrac{1}{4}\pi\rho\phi_1^3\phi_2\left(\zeta_{1t} + v\zeta_{1z} + \zeta_1^2\right)\\
&\quad = p + \phi_1\phi_2 h(\phi_1,\phi_2) - 2\mu\pi\phi_1\phi_2\zeta_1 + \tfrac{1}{4}\mu\pi\left(\phi_1^3\phi_2\zeta_{1z}\right)_z,\\
&\tfrac{1}{4}\pi\rho\phi_2^3\phi_1\left(\zeta_{2t} + v\zeta_{2z} + \zeta_2^2\right)\\
&\quad = p + \phi_1\phi_2 h(\phi_2,\phi_1) - 2\mu\pi\phi_1\phi_2\zeta_2 + \tfrac{1}{4}\mu\pi\left(\phi_2^3\phi_1\zeta_{2z}\right)_z,\\
&\pi\rho\phi_1\phi_2(v_t + vv_z)\\
&\quad = -p_z - \phi_2\phi_{1z}h(\phi_1,\phi_2) - \phi_1\phi_{2z}h(\phi_2,\phi_1)\\
&\qquad + 2\mu\pi(\phi_1\phi_2 v_z)_z.
\end{aligned} \tag{3}$$

Here, ρ is the constant fluid density, μ is the constant fluid viscosity, and $p = (\bar{p} - p_0)\pi\phi_1\phi_2$, where p_0 is the constant external pressure and $\bar{p}$ is the mean pressure averaged over a cross section of the jet. Especially, the surface tension force term $h(\phi_1,\phi_2)=\int_0^{2\pi}\sigma q(\phi_1,\phi_2)\cos^2\theta d\theta$, where σ is the surface tension coefficient, and $q(\phi_1,\phi_2)$ is the mean curvature of the elliptical cross section. In the nonsymmetric jet problem this h term is the key parameter that leads to axis-switching. Geometrically, the jet cross section can be described by an angular coordinate θ ranging from 0 to 2π, which is related to the elliptic parameter equation as

$$x=\phi_1\cos\theta,\quad y=\phi_2\sin\theta. \tag{4}$$

Thus, the mean curvature $q(\phi_1,\phi_2)$ of the elliptical cross section can be formulated as

$$\begin{aligned} q(\phi_1,\phi_2) = {} & \left[(\phi_1\phi_{2z}\sin^2\theta+\phi_2\phi_{1z}\cos^2\theta)^2+\phi_1^2\sin^2\theta+\phi_2^2\cos^2\theta\right]^{-1.5}\left[\left(\phi_1^2\sin^2\theta+\phi_2^2\cos^2\theta\right)(\phi_2\phi_{1zz}\cos^2\theta+\phi_1\phi_{2zz}\sin^2\theta)\right. \\ & \left.+2(\phi_1\phi_{2z}-\phi_2\phi_{1z})(\phi_1\phi_{1z}-\phi_2\phi_{2z})\sin^2\theta\cos^2\theta-\phi_1\phi_2\left(\phi_{1z}^2\cos^2\theta+\phi_{2z}^2\sin^2\theta+1\right)\right]. \end{aligned} \tag{5}$$

To analyze Eqs. (1) and (3), we assume the disturbances are relatively small compared with the mean quantities. Taking the following variable decompositions,

$$\phi_1=a+\bar{\phi}_1,\quad \phi_2=b+\bar{\phi}_2,\quad v=V+\bar{v}. \tag{6}$$

Here, a and b are the initial semimajor and semiminor radius, respectively, and V is mean velocity along the z axis. Define the orifice aspect ratio as $e=b/a$. Under the condition that the jet is close to being circular or $e\simeq 1$, the $\bar{}$ terms are much smaller than the primary ones. Therefore, the nonlinear terms in the momentum equation can be linearized as

$$\begin{aligned} \zeta_{1t}+v\zeta_{1z}+\zeta_1^2 &= \frac{a(\bar{\phi}_{1tt}+2V\bar{\phi}_{1zt}+V^2\bar{\phi}_{1zz})}{\phi_1^2}, \\ \zeta_{2t}+v\zeta_{2z}+\zeta_2^2 &= \frac{b(\bar{\phi}_{2tt}+2V\bar{\phi}_{2zt}+V^2\bar{\phi}_{2zz})}{\phi_2^2}, \\ 2\mu\pi\phi_1\phi_2\zeta_1 &= 2\mu\pi b(\bar{\phi}_{1t}+V\bar{\phi}_{1z}), \\ 2\mu\pi\phi_1\phi_2\zeta_2 &= 2\mu\pi a(\bar{\phi}_{2t}+V\bar{\phi}_{2z}), \\ \frac{1}{4}\mu\pi(\phi_1^3\phi_2\zeta_{1z})_z &= \frac{1}{4}\mu\pi a^2b(\bar{\phi}_{1tzz}+V\bar{\phi}_{1zzz}), \\ \frac{1}{4}\mu\pi(\phi_2^3\phi_1\zeta_{2z})_z &= \frac{1}{4}\mu\pi ab^2(\bar{\phi}_{2tzz}+V\bar{\phi}_{2zzz}), \\ v_t+vv_z &= \bar{v}_t+V\bar{v}_z, \end{aligned} \tag{7}$$

$$\begin{aligned} h(\phi_1,\phi_2) &= \int_0^{2\pi}\sigma\frac{[(a^2\sin^2\theta+b^2\cos^2\theta)(\bar{\phi}_{1zz}b\cos^2\theta+\bar{\phi}_{2zz}a\sin^2\theta)-(ab+a\bar{\phi}_2+b\bar{\phi}_1)]}{[(a^2+2a\bar{\phi}_1)\sin^2\theta+(b^2+2b\bar{\phi}_2)\cos^2\theta]^{1.5}}\cos^2\theta d\theta, \\ h(\phi_2,\phi_1) &= \int_0^{2\pi}\sigma\frac{[(a^2\cos^2\theta+b^2\sin^2\theta)(\bar{\phi}_{2zz}a\cos^2\theta+\bar{\phi}_{1zz}b\sin^2\theta)-(ab+a\bar{\phi}_2+b\bar{\phi}_1)]}{[(a^2+2a\bar{\phi}_1)\cos^2\theta+(b^2+2b\bar{\phi}_2)\sin^2\theta]^{1.5}}\cos^2\theta d\theta. \end{aligned} \tag{8}$$

Using the Taylor expansion with respect to small perturbation, Eqs. (8) can be expressed as

$$\begin{aligned} h(\phi_1,\phi_2) &= k_1+k_2\bar{\phi}_1+k_3\bar{\phi}_2+k_4\bar{\phi}_{1zz}+k_5\bar{\phi}_{2zz}, \\ h(\phi_2,\phi_1) &= k_1'+k_2'\bar{\phi}_1+k_3'\bar{\phi}_2+k_4'\bar{\phi}_{1zz}+k_5'\bar{\phi}_{2zz}, \end{aligned} \tag{9}$$

where the expressions for k_i and k_i' can be found in Eqs. (A1) and (A2). Therefore, the terms containing h are

$$\begin{aligned} \phi_1\phi_2h(\phi_1,\phi_2) &= n_1+n_2\bar{\phi}_1+n_3\bar{\phi}_2+n_4\bar{\phi}_{1zz}+n_5\bar{\phi}_{2zz}, \\ \phi_1\phi_2h(\phi_2,\phi_1) &= m_1+m_2\bar{\phi}_1+m_3\bar{\phi}_2+m_4\bar{\phi}_{1zz}+m_5\bar{\phi}_{2zz}. \end{aligned} \tag{10}$$

Finally, the linearized continuity equation and momentum equations along the x, y, and z directions are

$$\begin{aligned} & \frac{\bar{\phi}_{1t}}{a}+V\frac{\bar{\phi}_{1z}}{a}+\frac{\bar{\phi}_{2t}}{b}+V\frac{\bar{\phi}_{2z}}{b}+\bar{v}_z=0, \\ & -\frac{1}{4}\pi\rho a^2b(\bar{\phi}_{1tt}+2V\bar{\phi}_{1zt}+V^2\bar{\phi}_{1zz})+\bar{p}+n_1+n_2\bar{\phi}_1+n_3\bar{\phi}_2+n_4\bar{\phi}_{1zz}+n_5\bar{\phi}_{2zz}-2\mu\pi b(\bar{\phi}_{1t}+V\bar{\phi}_{1z}) \\ & \quad +\frac{1}{4}\mu\pi a^2b(\bar{\phi}_{1tzz}+V\bar{\phi}_{1zzz})=0, \end{aligned}$$

$$\begin{aligned}
&-\frac{1}{4}\pi\rho ab^2(\bar{\phi}_{2tt}+2V\bar{\phi}_{2zt}+V^2\bar{\phi}_{2zz})+\bar{p}+m_1+m_2\bar{\phi}_1+m_3\bar{\phi}_2+m_4\bar{\phi}_{1zz}+m_5\bar{\phi}_{2zz}-2\mu\pi a(\bar{\phi}_{2t}+V\bar{\phi}_{2z})\\
&\quad+\frac{1}{4}\mu\pi ab^2(\bar{\phi}_{2tzz}+V\bar{\phi}_{2zzz})=0,\\
&-\pi\rho ab(\bar{v}_t+V\bar{v}_z)-\bar{p}_z-bk_1\bar{\phi}_{1z}-ak'_1\bar{\phi}_{2z}+2\mu\pi ab\bar{v}_{zz}=0.
\end{aligned}\tag{11}$$

Details of the derivation and the expressions for n_i,m_i ($i = 1$–5) are in Eqs. (A3).

In stability analysis the perturbation modes are assumed as

$$\bar{\phi}_1 = f_1(k,\omega)\exp[i(\omega t-kz)],\quad \bar{\phi}_2 = f_2(k,\omega)\exp[i(\omega t-kz)],\tag{12}$$

where k and ω are the wave number and angular frequency, respectively. For this spatial instability rather than temporal instability problem [27], the disturbances grow along the spatial z direction instead of t, which then implies that the k need to have a nonzero imaginary part, while ω does not.

To find the solution, first we need to remove the pressure term p. By integrating the last subequation in Eqs. (11) with respect to z to remove the pressure, we then obtain the nonhomogeneous linear equations as

$$\begin{aligned}
&-\frac{\pi}{4}\rho a^2b(\bar{\phi}_{1tt}+2V\bar{\phi}_{1zt}+V^2\bar{\phi}_{1zz})+[n_2+\pi\rho b\mathbb{T}-bk_1]\bar{\phi}_1+[n_3+\pi\rho a\mathbb{T}-ak'_1]\bar{\phi}_2+n_4\bar{\phi}_{1zz}+n_5\bar{\phi}_{2zz}\\
&\quad-4\pi\mu b(\bar{\phi}_{1t}+V\bar{\phi}_{1z})-2\pi\mu a(\bar{\phi}_{2t}+V\bar{\phi}_{2z})+\frac{\pi}{4}\mu a^2b(\bar{\phi}_{1tzz}+V\bar{\phi}_{1zzz})+n_1=0,\\
&-\frac{\pi}{4}\rho ab^2(\bar{\phi}_{2tt}+2V\bar{\phi}_{2zt}+V^2\bar{\phi}_{2zz})+[m_2+\pi\rho b\mathbb{T}-bk_1]\bar{\phi}_1+[m_3+\pi\rho a\mathbb{T}-ak'_1]\bar{\phi}_2+m_4\bar{\phi}_{1zz}+m_5\bar{\phi}_{2zz}\\
&\quad-4\pi\mu a(\bar{\phi}_{2t}+V\bar{\phi}_{2z})-2\pi\mu b(\bar{\phi}_{1t}+V\bar{\phi}_{1z})+\frac{\pi}{4}\mu ab^2(\bar{\phi}_{2tzz}+V\bar{\phi}_{2zzz})+m_1=0.
\end{aligned}\tag{13}$$

Here, $\mathbb{T} = (V - \frac{\omega}{k})^2$. We address that in the present analysis integrating Eqs. (11) is necessary to view the difference in the momentum relation along two principal directions, which, however, cannot be adequately described by the differentiation operation as in Ref. [17].

C. Boundary condition and solutions

The solution of the nonhomogeneous equation (13) consists of both the complementary solution part and the particular solution part. Simply enough, the particular solutions $\bar{\phi}_{1p}$ and $\bar{\phi}_{2p}$ are

$$\bar{\phi}_{1p} = -a,\quad \bar{\phi}_{2p} = -b.\tag{14}$$

Meanwhile, the complementary solution $\bar{\phi}_{1c}$ and $\bar{\phi}_{2c}$ for the homogeneous part of Eqs. (13) satisfies

$$A_1\bar{\phi}_{1c}+A_2\bar{\phi}_{2c}=0,\quad A_3\bar{\phi}_{1c}+A_4\bar{\phi}_{2c}=0,\tag{15}$$

Details of A_i ($i = 1,2,3,4$) are in Eqs. (A4).

The dispersion relation between the wave number and frequency is determined from the nonzero solution of Eqs. (15), which implies a zero determinant of the coefficient matrix ($A_1A_4 - A_2A_3 = 0$) as

$$\sum_{i=0}^{10} a_i k^i = 0,\tag{16}$$

where a_i are defined in Eqs. (A6). Equation (16) has ten roots. According to the analysis by Bogy [26], physically, the wave propagation and the roots of the dispersion equation need to satisfy the radiation condition, which means the disturbance wave and its energy must propagate outside to infinity. In other words, both the phase velocity ($v_p = \omega/k_r$) and group velocity ($v_g = d\omega/dk_r$) need to be positive, where k_r is the real part of the wave number k. If we set $\omega = 0$ in Eq. (16), both k_1 and k_2 are equal to zero. When $\omega \neq 0$, we obtain two complex conjugates k_1 and k_2. Specifically, the positive imaginary part means along the z direction the spatial growth rate, while the negative one means the spatial damping rate.

In the present jet problem a special state is $V = 0$, at which Eq. (16) can be regarded as the temporal dispersion equation. Retaining only the nonzero parts, Eq. (16) becomes

$$\sum_{j=0}^{4} b_j\omega^j = 0,\tag{17}$$

where the coefficients b_j are listed in Eq. (A7) in the Appendix. Here, Eq. (17) has four roots, two of which need to be removed due to the same radiation argument, and the other two are purely imaginary. For this temporal instability problem ($V = 0$) the nondimensional temporal growth rate can be defined as $\alpha = \omega i\sqrt{\rho R^3/\sigma}$, where R is the equivalent radius defined as $R = (ab)^{1/2}$. As shown in Fig. 3, this result coincides exactly with Rayleigh's temporal solution, which is derived differently from the velocity potential equation.

For general $V \neq 0$ cases, we define the dimensionless parameters as $\tilde{z} = z/R$, $\tilde{t} = Vt/R$, $\tilde{\delta}_1 = \bar{\phi}_1/a$, $\tilde{\delta}_2 = \bar{\phi}_2/b$, $\tilde{v} = \bar{v}/V$, $\tilde{\delta}_{1p} = \bar{\phi}_{1p}/a$, $\tilde{\delta}_{2p} = \bar{\phi}_{2p}/b$, $\beta = \omega R/V$, and wave number $K = kR$. In the following, for simplicity, the tildes are omitted. Thus, the final solution is the sum of the particular solution and a linear combination of all possible complementary solutions from Eqs. (15). We then obtain

$$\begin{aligned}
\delta_1 = &\sum_{\beta=0}^{\beta_c}\{C_1\exp[i(\beta t-K_1z)]+C_2\exp[i(\beta t-K_2z)]\}\\
&+\{C_3\exp(-iK_3z)+\delta_{1p}\},
\end{aligned}$$

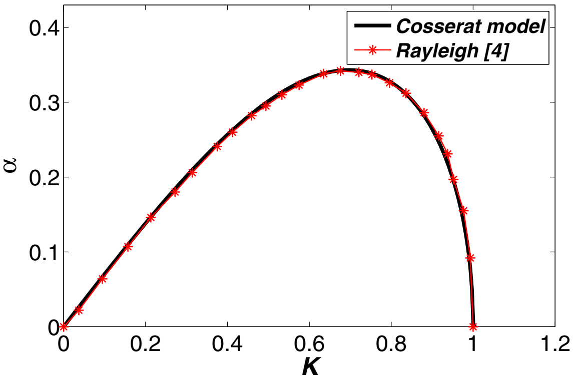

FIG. 3. Comparison of the temporal solution obtained from the Cosserat equation in the present analysis and the Rayleigh's relation [4].

$$\delta_2 = \sum_{\beta=0}^{\beta_c}\{D_1 \exp[i(\beta t - K_1 z)] + D_2 \exp[i(\beta t - K_2 z)]\} + \{D_3 \exp(-iK_3 z) + \delta_{2p}\}, \qquad (18)$$

where C_i and D_i $(i = 1,2,3)$ are the constant coefficients to be determined by the boundary conditions, β_c is the cutoff frequency which means the jet is stable when $\beta > \beta_c$, and K_3 is the only one positive real wave number corresponding to $\beta = 0$ (the complex k_3 is not a physical solution). More important physics related to this part will be discussed later.

Using the coefficients a_i listed in the Appendix, we find that in Eqs. (15), $\bar{\phi}_2/\bar{\phi}_1 = 1$ always holds for K_1 and K_2, and $\bar{\phi}_2/\bar{\phi}_1 = -e$ for K_3, independent of the value of V, μ, σ and ρ. Therefore, it yields the following ratio relations,

$$D_1/C_1 = D_2/C_2 = 1/e, \quad D_3/C_3 = -1. \qquad (19)$$

In the present semi-infinite jet problem, the shape of the elliptic orifice is fixed at the jet outlet, where the jet flow is harmonically forced along the mean flow direction, e.g., to be achieved using a pulse generator with an excited voltage and frequency. Thus, we have the following boundary conditions,

$$\delta_1(0,t) = 0, \quad \delta_2(0,t) = 0, \quad v(0,t) = v_f \cos\beta_f t. \qquad (20)$$

It needs to be mentioned that to match the frequency condition between the nozzle outlet and the forced $v(0,t)$ disturbance boundary condition, the frequency of the harmonic mode in Eqs. (18) must be β_f as well, hence other different modes need to excluded. Meanwhile, the $\beta = 0$ part in Eqs. (18) is necessary to satisfy such boundary conditions. Therefore, the jet profile has only the β_f and $\beta = 0$ parts. Combining Eqs. (19) and (20), the final expressions of the perturbations is

$$\delta_1 = \frac{v_f K_1 K_2}{\left(1+\frac{1}{e}\right)\beta_f (K_2 - K_1)}\{\exp[i(\beta_f t - K_1 z)] - \exp[i(\beta_f t - K_2 z)]\} + \frac{1-e}{1+e}\{\exp[-i(K_3 z)] - 1\},$$

$$\delta_2 = \frac{v_f K_1 K_2}{e\left(1+\frac{1}{e}\right)\beta_f (K_2 - K_1)}\{\exp[i(\beta_f t - K_1 z)] - \exp[i(\beta_f t - K_2 z)]\} + \frac{e-1}{1+e}\{\exp[-i(K_3 z)] - 1\}. \qquad (21)$$

This result has the following important meanings. Overall, there are two different contributions in this relation, the part related to the external perturbation with v_f and β_f, and the part related to K_3. The former part shows how the external perturbation evolves with t and z. The conjugates K_1 and K_2 represent the growth rate and damping rate of the perturbation, respectively. Physically, the jet will break up when the amplitude of perturbations equals the jet minor radius. If the liquid is inviscid, K_3 is a real number, and for the viscous case, K_3 is complex. Thus, the K_3 part means an oscillating wave, neither damped nor excited, independent of external perturbation. Physically, this solution suggests a kind of natural instability from the axis-switching phenomenon. From the coefficient $\frac{e-1}{1+e}$ it is easy to see that this part vanishes for the circular jet case with $e = 1$. The larger the deviation of e from unity, the stronger the axis-switching will be. Because of the particular solution of Eqs. (13), mathematically, the K_3 term must exist in order to satisfy the orifice boundary conditions. Therefore, the axis-switching is an inherent feature of nonsymmetrical jets. Because of dissipation of fluid viscosity, axis-switching typically appears in the early stage of the elliptic jet flow and will be damped far downstream, if the jet remains integrated. In the experiment of an elliptical water-glycerol mixture jet with a relatively larger viscosity, the jet finally tends to be circular [8]. In summary, the external perturbation part and the axis-switching part are independent and controlled by different physical mechanisms. The local unbalanced capillary force, which is characterized by the e parameter, determines the relative importance of axis-switching to the overall disturbance evolution.

III. RESULTS AND ANALYSIS

A. Effects from the operation parameters

To verify the theoretical predictions, the initial elliptic jets emanating from the elliptic nozzles have been investigated experimentally. Figure 4 shows the experiment schematic. A manual valve is used to regulate the flow of nitrogen gas in a compressed bottle, which is used to pressurize the de-ionized water in the accumulator. The water supplied to the drop generator is controlled by the pulse width modulated (PWM) electrical signal of a function generator (ATTEN, ATF 20B) in a sinusoidal wave form. A high-intensity xenon arc lamp (Newport 67005) provides the necessary illumination for recording the liquid jet behavior. The backlit imaging technique is utilized and a semi-transparent screen is placed between the liquid jet and the high-intensity illuminator to facilitate a uniform background for imaging the initial formation of the liquid jet. By using image analysis, the jet characteristic parameters, including the wavelength and wave amplitude, can be measured.

As shown in Fig. 5(a), the major axes oscillate periodically, which then determines the wavelength of axis-switching. The

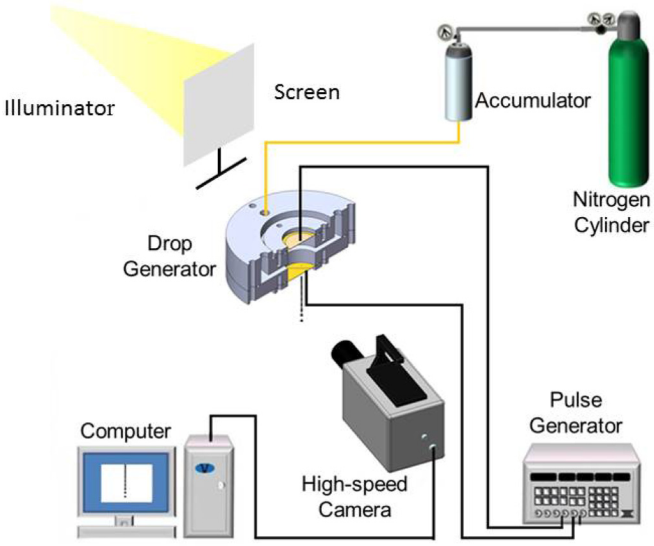

FIG. 4. Schematic of the overall experimental setup.

wavelength λ is calculated via the relation $\lambda = 2\pi/k_3$. It needs to be mentioned that near the jet outlet, because of the inertial influences from the nozzle structure, to some extent the axis-switching structure could be ambiguous, which can be avoided by measuring the wavelength somewhere downstream.

In the experiment the jet velocity V can be determined straightforwardly by the mass flow rate, which is, however, not convenient in real operation. Alternatively, the jet pressure P is adopted to estimate V based on the Bernoulli relation $P = \rho V^2/2$. The results in Fig. 5(b), showing a good match between these two different methods, justify the accuracy of such an estimation.

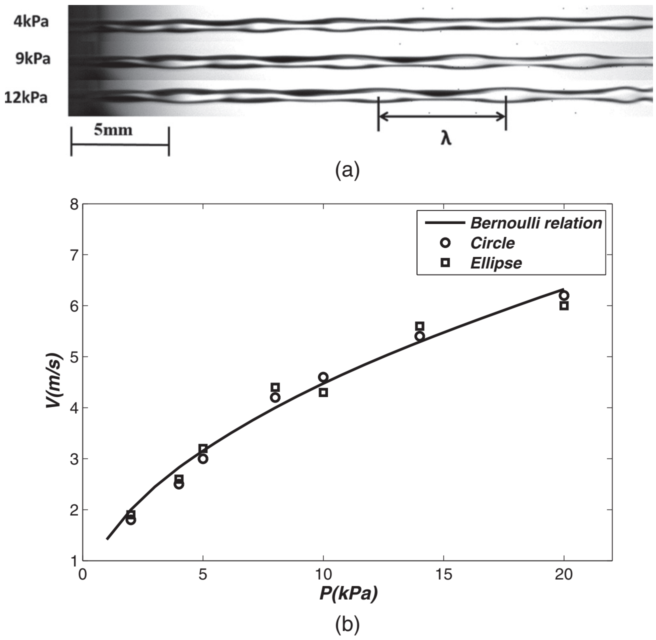

FIG. 5. (a) Experimental observation of axis-switching for the elliptic jet at different pressures. (b) Relation of pressure and jet outlet velocity.

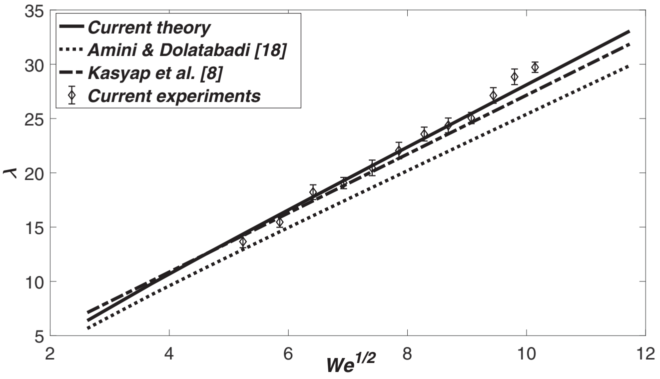

FIG. 6. Comparison between theoretical and experimental results of the dependence of the axis-switching wavelength on the jet pressure. The error bars shown here are from 30 repetitions of the measurements under the same conditions, together with existing results [8,18].

From Eq. (16) the coefficients a_i are the function of frequency, jet velocity, and other parameters. For natural axis-switching, the external excitation frequency is set to be zero. Thus, the dependence of wavelength on the Weber number, which is a function of the jet velocity or pressure, can be numerically calculated. Figure 6 shows satisfactory agreement between the present theory and measurement results, where the error bars are from 30 repetitions under the same conditions. Overall, the wavelength increases almost linearly with the square root of the Weber number. In addition, we also include in Fig. 6 the fitting curve with experimental measurements [8] and the existing formula [18] for an inviscid jet with small aspect ratios. Overall, the current theory agrees well with the results in our measurement regime, while the formula in Ref. [18] shows a clear underprediction.

The present analysis also indicates that the axis-switching wavelength is independent of external disturbances. Figures 7(a) and 7(b) show the axis-switching structure by changing the disturbance amplitude, which is controlled by the

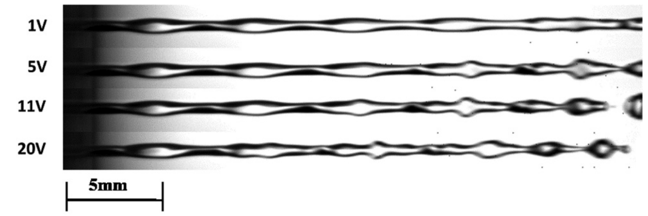

(a) inlet pressure:$7kPa$, forced frequency:$1800Hz$

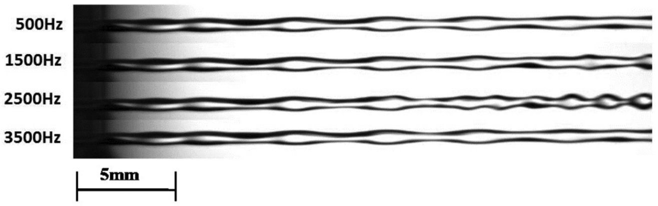

(b) inlet pressure:$7kPa$, forced voltage:$2V$

FIG. 7. The effects of (a) forced voltage and (b) frequency on the axis-switching structure. In a large variation range of the controlling parameters, the wavelength of axis-switching remains almost constant.

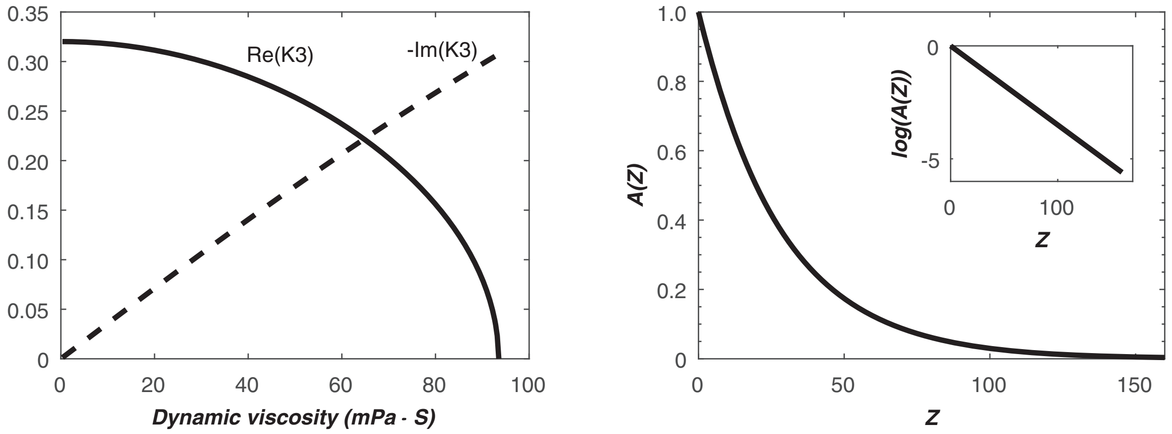

(a)

(b)

FIG. 8. (a) The change of real [Re(K_3)] and imaginary [Im(K_3)] parts of K_3 with the fluid viscosity at We = 100. (b) In physical space the variation of the dimensionless amplitude $A(Z)$ with Z at $P = 10$ kPa and 12 mPa s dynamic viscosity.

voltage imposed onto the jet, and the frequency of the noise, respectively. Clearly, in a large variation range the wavelength remains constant.

B. Effects from the fluid viscosity

Existing results related to the viscosity effects are very limited. For the inviscid case, K_3 in Eqs. (18) is real, while for the viscous case, K_3 is complex with a real part Re(K_3) and a negative imaginary part Im(K_3). As shown in Fig. 8(a), at a typical We = 100 with an increase of viscosity, the Re(K_3) decreases and $-$Im(K_3) increases, which implies the damping effect of viscosity becomes stronger. In the physical space the damping rate can be easily calculated from Im(K_3). As shown in Fig. 8(b), under a typical condition, the variation of the dimensionless amplitude $A(Z)$ with Z decays exponentially because of the energy dissipation by fluid viscosity.

Experimentally, the variation of the jet structure in Fig. 9 illustrates that with an increase of fluid viscosity, the axis-switching amplitude decays more rapidly. Specifically, when the mass concentration of glycerol is 10%, axis-switching almost sustains in the measurement range; for the 50% concentration case, axis-switching exists clearly in the first few oscillation periods and then decays to vanishing; if the glycerol concentration is as high as 70%, axis-switching is almost entirely damped.

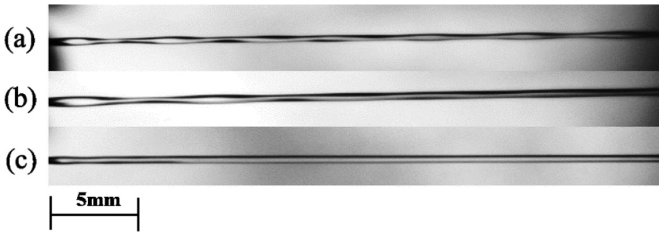

FIG. 9. The damping effect of elliptic jets with glycerol mass concentrations of (a) 10%, (b) 50%, and (c) 70%.

C. Dispersion relations

According to the theoretical prediction [Eq. (16)], we can also have a parametric study of the dispersion relation. Setting the Ohnesorge number $\mathrm{Oh} = \mu/\sqrt{\rho R \sigma} = 0$ (the inviscid case) and the Weber number $\mathrm{We} = \rho R V^2/\sigma = 50$, the relation of nondimensional frequency $\beta = \omega R/V$ and wave number $K = kR$ can be calculated numerically. The spatial instability is controlled by Im(K), the imaginary part of K. For the conjugate pair K_1 and K_2, only the one with the positive imaginary, e.g., Im(K_1), needs to be studied because it is responsible for the instability evolution.

Considering the influence from the aspect ratio e, Fig. 10(a) indicates that eccentricity reduces the growth rate of disturbances, while optimal β corresponding to the largest growth rate remains almost the same. It is similarly pointed out [13] that the spatial growth rate of symmetric disturbances decreases by making the nozzle more eccentric for inviscid and incompressible elliptic jets. Morris [14] further depicted the dispersion diagram which indicated almost the same optimal frequency corresponding to a maximum growth rate and cutoff frequency for symmetric disturbances. Although the maximum growth rate becomes smaller if e decrease, the ellipse structure may still be advantageous for jet breakup, because the smaller minor axis reduces the distance at which the perturbation amplitude equals the minor axis, i.e., the breakup condition. Results from Refs. [17,18] seem to significantly overestimate the growth rate and cutoff frequency [19]. The present results are consistent with a recent analysis [19]. Specifically, if the influence from the surrounding gas is neglected, the cutoff wave number is almost independent of the aspect ratio e.

Figure 10(b) shows the effect of liquid viscosity on the dispersion relation. As is expected, viscosity dampens the growth rate. The optimal frequency decreases as well. This result can be explained by the fact that dissipation is sensitive to frequency. At a larger viscosity, the frequency needs to be smaller to reduce dissipation for instability evolution.

The Weber number We measures the relative importance of the fluid inertia to the capillary forces. Figure 10(c)

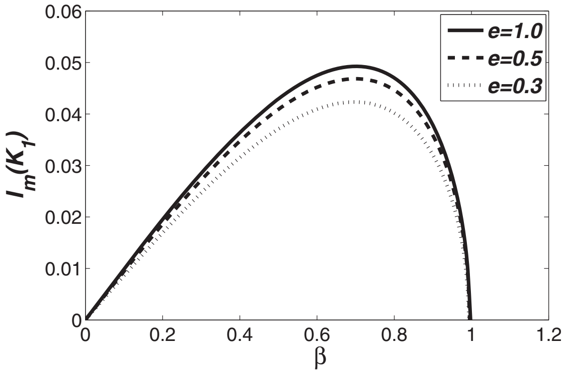

(a) $We = 50, Oh = 0$

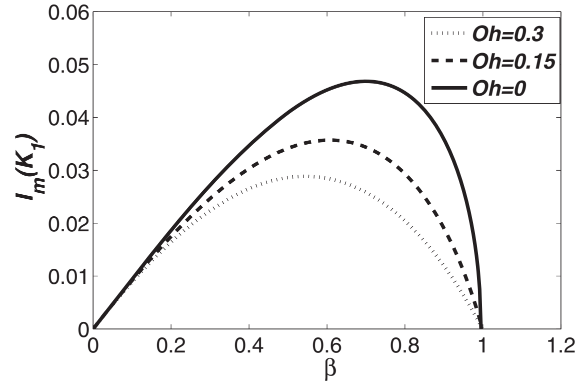

(b) $We = 50, e = 0.5$

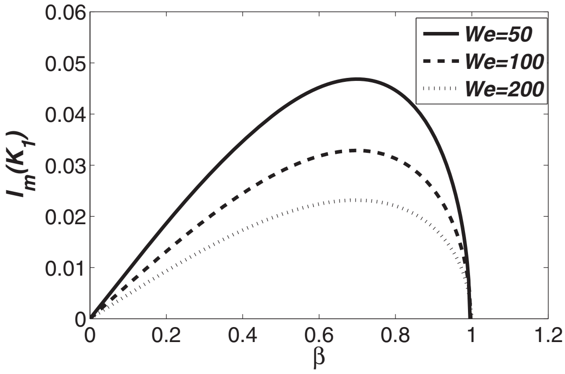

(c) $e = 0.5, Oh = 0$

FIG. 10. The dependence of the dispersion relation on (a) the orifice aspect ratio e, (b) the Ohnesorge number, and (c) the Weber number.

demonstrates that with an increase of We, the instability growth rate decreases. Experimentally, it is also concluded that increasing the jet velocity leads to a larger breakup length [8].

IV. CONCLUSIONS

In summary, linearized Cosserat equations that describe the viscous elliptic liquid jet have been analyzed to understand the instability evolution. Mathematically, the solution includes two parts, the complementary solution and the particular solution. The dispersion relation can be derived from the complementary solution. For disturbance modes with nonzero frequency, the wave number has two complex conjugate roots: One corresponds to the growth rate and the other corresponds to the damping rate. The contribution from these two waves is responsible for the jet breakup. Meanwhile, from the boundary condition of the orifice with unequal major axes, a nonzero particular solution must exist, which needs to be balanced by a spatial wave independent of the external perturbations. Physically, such a spatial wave corresponds to the axis-switching phenomena, inherent to nonsymmetric jet cases. In contrast, for a circular jet, the precoefficient of the spatial wave and particular solution part equals zero and therefore the axis-switching phenomenon vanishes.

Prediction of the axis-switching wavelength from the analytical solutions have been successfully verified with experimental measurements, including effects from the jet velocity, the fluid viscosity, and the forced disturbance parameters. Moreover, the dispersion relations have also been discussed. Present analyses predict quantitatively how the growth rate of spatial instability is influenced by orifice eccentricity, the Weber number, and the liquid viscosity (in the form of the Ohnesorge number Oh).

ACKNOWLEDGMENTS

The authors are thankful for experimental support from the Fuel Injection Spray Laboratory, National Engineering Laboratory for Automotive Electronic Control Technology, Institute of Automotive Engineering, SJTU. L.W. acknowledges funding support by National Science Foundation China (NSFC) under Grant No. 91441116, NSFC-CNRS joint research project (No. 11611130099, NSFC China, and PRC 2016-2018 LATUMAR “Turbulence lagrangienne: études numériques et applications environnementales marines,” CNRS, France).

APPENDIX: SOME ANALYTICAL REMARKS

In Eqs. (9) the coefficients can be determined from the Taylor expansion as

$$\begin{aligned}
k_1 &= -\sigma b E_1/a^2,\\
k_2 &= \sigma e(-E_1 + 3E_2)/a^2,\\
k_3 &= \sigma(-E_1 + 3e^2 E_2)/a^2,\\
k_4 &= \sigma e E_4,\\
k_5 &= \sigma E_5,\\
k_1' &= -\sigma b E_1'/a^2,\\
k_2' &= \sigma e(-E_1' + 3E_3')/a^2,\\
k_3' &= \sigma(-E_1' + 3e^2 E_2')/a^2,\\
k_4' &= \sigma e E_5',\\
k_5' &= \sigma E_4',
\end{aligned} \tag{A1}$$

and

$$\begin{aligned}
E_1 &= \int_0^{2\pi} \frac{\cos^2\theta}{(\sin^2\theta + e^2\cos^2\theta)^{1.5}} d\theta,\\
E_2 &= \int_0^{2\pi} \frac{\sin^2\theta\cos^2\theta}{(\sin^2\theta + e^2\cos^2\theta)^{2.5}} d\theta,\\
E_3 &= \int_0^{2\pi} \frac{\cos^4\theta}{(\sin^2\theta + e^2\cos^2\theta)^{2.5}} d\theta,\\
E_4 &= \int_0^{2\pi} \frac{\cos^4\theta}{(\sin^2\theta + e^2\cos^2\theta)^{0.5}} d\theta,\\
E_5 &= \int_0^{2\pi} \frac{\sin^2\theta\cos^2\theta}{(\sin^2\theta + e^2\cos^2\theta)^{0.5}} d\theta,\\
E_1' &= \int_0^{2\pi} \frac{\cos^2\theta}{(e^2\sin^2\theta + \cos^2\theta)^{1.5}} d\theta,\\
E_2' &= \int_0^{2\pi} \frac{\sin^2\theta\cos^2\theta}{(e^2\sin^2\theta + \cos^2\theta)^{2.5}} d\theta,\\
E_3' &= \int_0^{2\pi} \frac{\cos^4\theta}{(e^2\sin^2\theta + \cos^2\theta)^{2.5}} d\theta,\\
E_4' &= \int_0^{2\pi} \frac{\cos^4\theta}{(e^2\sin^2\theta + \cos^2\theta)^{0.5}} d\theta,\\
E_5' &= \int_0^{2\pi} \frac{\sin^2\theta\cos^2\theta}{(e^2\sin^2\theta + \cos^2\theta)^{0.5}} d\theta.
\end{aligned} \tag{A2}$$

The coefficients in Eqs. (11) can be defined as

$$\begin{aligned}
n_1 &= -\sigma a e^2 E_1,\\
n_2 &= \sigma e^2(-2E_1 + 3E_2),\\
n_3 &= \sigma e(-2E_1 + 3e^2 E_3),\\
n_4 &= \sigma a^2 e^2 E_4,\\
n_5 &= \sigma a^2 e E_5,\\
m_1 &= -\sigma a e^2 E_1',\\
m_2 &= \sigma e^2(-2E_1' + 3E_3'),\\
m_3 &= \sigma e(-2E_1' + 3eE_2'),\\
m_4 &= \sigma a^2 e^2 E_5',\\
m_5 &= \sigma a^2 e E_4'.
\end{aligned} \tag{A3}$$

To ensure a nontrivial solution, the coefficients need to satisfy

$$\begin{aligned}
A_1 &= k^{-2}(a_{15}k^5 + a_{14}k^4 + a_{13}k^3 + a_{12}k^2 + a_{11}k + a_{10}),\\
A_2 &= k^{-2}(a_{24}k^4 + a_{23}k^3 + a_{22}k^2 + a_{21}k + a_{20}),\\
A_3 &= k^{-2}(a_{34}k^4 + a_{33}k^3 + a_{32}k^2 + a_{31}k + a_{30}),\\
A_4 &= k^{-2}(a_{45}k^5 + a_{44}k^4 + a_{43}k^3 + a_{42}k^2 + a_{41}k + a_{40}),
\end{aligned} \tag{A4}$$

where

$$\begin{aligned}
a_{15} &= \frac{\pi}{4}\mu a^2 bVi,\\
a_{14} &= -\frac{\pi}{4}\mu a^2 b\omega i + \frac{\pi}{4}\rho a^2 bV^2 - n_4,\\
a_{13} &= -\frac{\pi}{2}\rho a^2 bV\omega + 4\pi\mu bVi,\\
a_{12} &= \frac{\pi}{4}\rho a^2 b\omega^2 - bk_1 + n_2 - 4\pi\mu b\omega i + \pi\rho bV^2,\\
a_{11} &= -2\pi\rho bV\omega,\\
a_{10} &= \pi\rho b\omega^2,\\
a_{24} &= -n_5,\\
a_{23} &= 2\pi\mu aVi,\\
a_{22} &= -ak'_1 + n_3 - 2\pi\mu a\omega i + \pi\rho aV^2,\\
a_{21} &= -2\pi\rho aV\omega,\\
a_{20} &= \pi\rho a\omega^2,\\
a_{34} &= -m_4,\\
a_{33} &= 2\pi\mu bVi,\\
a_{32} &= -bk_1 + m_2 - 2\pi\mu b\omega i + \pi\rho bV^2,\\
a_{31} &= -2\pi\rho bV\omega,\\
a_{30} &= \pi\rho b\omega^2,\\
a_{45} &= \frac{\pi}{4}\mu ab^2 Vi,\\
a_{44} &= -\frac{\pi}{4}\mu ab^2\omega i + \frac{\pi}{4}\rho ab^2 V^2 - m_5,\\
a_{43} &= -\frac{\pi}{2}\rho ab^2 V\omega + 4\pi\mu aVi,\\
a_{42} &= \frac{\pi}{4}\rho ab^2\omega^2 - ak'_1 + m_3 - 4\pi\mu a\omega i + \pi\rho aV^2,\\
a_{41} &= -2\pi\rho aV\omega,\\
a_{40} &= \pi\rho a\omega^2.
\end{aligned} \tag{A5}$$

The coefficients of spatial dispersion equations can then be determined as

$$\begin{aligned}
a_0 &= a_{10}a_{40} - a_{20}a_{30},\\
a_1 &= a_{11}a_{40} + a_{10}a_{41} - a_{21}a_{30} - a_{20}a_{31},\\
a_2 &= a_{12}a_{40} + a_{11}a_{41} + a_{10}a_{42} - a_{22}a_{30} - a_{21}a_{31} - a_{20}a_{32},\\
a_3 &= a_{13}a_{40} + a_{12}a_{41} + a_{11}a_{42} + a_{10}a_{43} - a_{23}a_{30}\\
&\quad - a_{22}a_{31} - a_{21}a_{32} - a_{20}a_{33},\\
a_4 &= a_{14}a_{40} + a_{13}a_{41} + a_{12}a_{42} + a_{11}a_{43} + a_{10}a_{44}\\
&\quad - a_{24}a_{30} - a_{23}a_{31} - a_{22}a_{32} - a_{21}a_{33} - a_{20}a_{34},\\
a_5 &= a_{15}a_{40} + a_{14}a_{41} + a_{13}a_{42} + a_{12}a_{43} + a_{11}a_{44}\\
&\quad + a_{10}a_{45} - a_{24}a_{31} - a_{23}a_{32} - a_{22}a_{33} - a_{21}a_{34},\\
a_6 &= a_{15}a_{41} + a_{14}a_{42} + a_{13}a_{43} + a_{12}a_{44} + a_{11}a_{45}\\
&\quad - a_{24}a_{32} - a_{23}a_{33} - a_{22}a_{34},\\
a_7 &= a_{15}a_{42} + a_{14}a_{43} + a_{13}a_{44} + a_{12}a_{45} - a_{24}a_{33} - a_{23}a_{34},\\
a_8 &= a_{15}a_{43} + a_{14}a_{44} + a_{13}a_{45} - a_{24}a_{34},\\
a_9 &= a_{15}a_{44} + a_{14}a_{45},\\
a_{10} &= a_{15}a_{45}.
\end{aligned} \tag{A6}$$

By setting $V = 0$ in Eq. (16) the coefficients of temporal dispersions in Eq. (17) are

$$\begin{aligned}
b_0 &= b_{10}b_{40} - b_{30}b_{20},\\
b_1 &= b_{11}b_{40} + b_{10}b_{41} - b_{31}b_{20} - b_{30}b_{21},\\
b_2 &= b_{12}b_{40} + b_{11}b_{41} + b_{10}b_{42} - b_{32}b_{20} - b_{31}b_{21} - b_{30}b_{22},\\
b_3 &= b_{12}b_{41} + b_{11}b_{42} - b_{32}b_{21} - b_{31}b_{22},\\
b_4 &= b_{12}b_{42} - b_{32}b_{22},
\end{aligned} \tag{A7}$$

where

$$\begin{aligned}
b_{12} &= \frac{\pi}{4}\rho a^2 b + \frac{\pi\rho b}{k^2},\\
b_{11} &= -4\pi\mu b i - \frac{\pi}{4}\mu a^2 b k^2 i,\\
b_{10} &= n_2 - bk_1 - n_4 k^2,\\
b_{22} &= \frac{\pi}{k^2}\rho a,\\
b_{21} &= -2\pi\mu a i,\\
b_{20} &= n_3 - ak_1' - n_5 k^2,\\
b_{32} &= \frac{\pi}{k^2}\rho b,\\
b_{31} &= -2\pi\mu b i,\\
b_{30} &= m_2 - bk_1 - m_4 k^2,\\
b_{42} &= \frac{\pi}{4}\rho a b^2 + \frac{\pi\rho a}{k^2},\\
b_{41} &= -4\pi\mu a i - \frac{\pi}{4}\mu a b^2 k^2 i,\\
b_{40} &= m_3 - ak_1' - m_5 k^2.
\end{aligned} \tag{A8}$$

[1] R. D. Reitz and F. B. Bracco, On the dependence of spray angle and other spray parameters on nozzle design and operating conditions, SAE Technical Paper No. 790494, 1979.

[2] F. Savart, Ann. Chem. Phys. **53**, 337 (1833).

[3] J. A. F. Plateau, in *Satique Experimentale Et Theoretique Des Liquid Soumie Aux Seuls Forces Molecularies. Canthier* (Gautier-Villers, Paris, 1873), Vol. 2, p. 518.

[4] Lord Rayleigh, Proc. R. Soc. London **29**, 71 (1879).

[5] C. Weber, Z. Angew. Math. Mech. **11**, 136 (1931).

[6] G. I. Taylor and L. Howarth, Proc. R. Soc. Lond. A **253**, 289 (1959).

[7] N. Ashgriz, A. L. Yarin, X. Li, A. Sarchami, A. Mashayek, and M. Movassat, *Handbook of Atomization and Sprays* (Springer, New York, 2011).

[8] T. V. Kasyap, D. Sivakumar, and B. N. Raghunandan, Int. J. Multiphase Flow **35**, 8 (2009).

[9] F. Shokoohi and H. G. Elrod, J. Comput. Phys. **71**, 324 (1987).

[10] F. J. Wang and T. G. Fang, Int. J. Multiphase Flow **72**, 248 (2015).

[11] D. A. Caulk and P. M. Naghdi, Arch. Ration. Mech. Anal. **69**, 1 (1979).

[12] D. A. Caulk and P. M. Naghdi, J. Appl. Mech. **46**, 291 (1979).

[13] D. Miller, in *AIAA 22nd Aerospace Sciences Meeting* (AIAA, Reston, VA, 1984).

[14] P. J. Morris, AIAA J. **26**, 172 (1986).

[15] S. E. Bechtel, M. G. Forest, D. D. Holm, and K. J. Lin, J. Fluid Mech. **196**, 241 (1988).

[16] S. E. Bechtel, J. Appl. Mech. **56**, 968 (1989).

[17] G. Amini and A. Dolatabadi, Phys. Fluids **23**, 084109 (2011).

[18] G. Amini and A. Dolatabadi, Int. J. Multiphase Flow **42**, 96 (2012).

[19] G. Amini, L. Yu, A. Dolatabadi, and M. Ihme, Phys. Fluids **26**, 114105 (2014).

[20] H. C. Lee, IBM J. Res. Dev. **18**, 364 (1974).

[21] A. E. Green, N. Laws, and P. M. Naghdi, Math. Proc. Cambridge Philos. Soc. **64**, 895 (1968).

[22] A. E. Green, P. M. Naghdi, and M. L. Wenner, Proc. R. Soc. Lond. A **337**, 485 (1974).

[23] A. E. Green and P. M. Naghdi, J. Fluid Mech. **78**, 237 (1976).

[24] W. T. Pimbley, IBM J. Res. Dev. **20**, 148 (1976).

[25] D. B. Bogy, Phys. Fluids **21**, 190 (1978).

[26] D. B. Bogy, J. Appl. Mech. **45**, 469 (1978).

[27] J. B. Keller, S. I. Rubinow, and Y. O. Tu, Phys. Fluids **16**, 2052 (1973).